



**CHALMERS**  
UNIVERSITY OF TECHNOLOGY

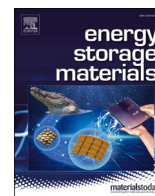
## Exploring the electrochemistry of PTCDI for aqueous lithium-ion batteries

Downloaded from: <https://research.chalmers.se>, 2024-03-20 08:52 UTC

Citation for the original published paper (version of record):

Brown, J., Karlsmo, M., Johansson, P. et al (2024). Exploring the electrochemistry of PTCDI for aqueous lithium-ion batteries. *Energy Storage Materials*, 66(103218).  
<http://dx.doi.org/10.1016/j.ensm.2024.103218>

N.B. When citing this work, cite the original published paper.



## Exploring the electrochemistry of PTCDI for aqueous lithium-ion batteries

John Brown<sup>a,b,c,1</sup>, Martin Karlsmo<sup>d,1</sup>, Ezzoubair Bendadesse<sup>a,b</sup>, Patrik Johansson<sup>c,d,\*</sup>,  
Alexis Grimaud<sup>a,b,e,\*\*</sup>

<sup>a</sup> Chimie du Solide et de l'Energie (CSE), Collège de France, UMR 8260, 75231 Paris Cedex 05, France

<sup>b</sup> Réseau sur le Stockage Electrochimique de l'Energie (RS2E), CNRS FR 3459, 80039 Amiens Cedex 1, France

<sup>c</sup> ALISTORE-ERI, CNRS FR 3104, Hub de l'Energie, 80039 Amiens Cedex, France

<sup>d</sup> Department of Physics, Chalmers University of Technology, 41296, Göteborg, Sweden

<sup>e</sup> Department of Chemistry, Boston College, Chestnut Hill, MA 02467, United States

## ARTICLE INFO

## Keywords:

Electrochemistry  
Lithium-ion batteries  
Aqueous electrolytes  
Organic active materials  
Sustainability

## ABSTRACT

Aqueous lithium-ion batteries (ALIBs) hold promise of providing cost-effective and safe energy storage in the context of an increasingly environmentally aware narrative. Moreover, mitigating concerns surrounding the critical raw materials present in traditional LIBs reinforces the alignment with such ideals. Herein, we delve into the electrochemistry of perylene-3,4,9,10-tetracarboxylic acid diimide (PTCDI) and evaluate its potential as an organic anode active material for ALIBs. We find the all-organic anode to reversibly (de)intercalate  $\text{Li}^+$  with moderately concentrated aqueous electrolytes, although in a slightly different manner compared with organic solvents. Furthermore, the half-cell electrochemical performance in terms of capacity, capacity retention, rate performance, Coulombic efficiency, and self-discharge, is all indeed satisfactory, where proof-of-concept ALIBs using the high voltage lithium manganese oxide (LMO) exhibit  $>70 \text{ Wh kg}^{-1}_{(\text{PTCDI}+\text{LMO})}$  and an average voltage of ca. 1.5 V. These findings have the intention to further encourage organic redox-active material R&D with more dilute aqueous electrolytes, potentially paving the way towards a greener and more sustainable energy landscape.

## Introduction

Driven by cost, environmental aspects, and safety considerations, the development of aqueous lithium-ion batteries (ALIBs) aims to provide a complementary energy storage solution to traditional LIBs [1]. Using organic active materials in tandem with the aqueous electrolytes is an even more attractive avenue, as these materials are composed of abundant elements, offering the promise of renewability and environmental friendliness, aligning with the green ethos of aqueous electrolytes [2,3]. Furthermore, the creation of such batteries aligns with the EU's critical raw materials directive, raising awareness of potential future shortages and price spikes of commercial LIB constituents; cobalt, natural graphite, lithium, nickel, copper and manganese [4], highlighting the need for new cell chemistries.

Using aqueous electrolytes, however, does come with inherent challenges [5]. The pool of active materials with redox potentials within the water splitting reaction range is severely limited, and moreover

many of these materials dissolve in aqueous media. Several polymers have previously been explored with rather good performance, yet the latter issue still remains for these batteries [6–8]. Perylene-type molecules are another family of compounds displaying excellent charge transport properties and cycling stability with both non-aqueous and aqueous electrolytes [9–11]. One such material is the commercially available organic pigment perylene-3,4,9,10-tetracarboxylic acid diimide (PTCDI), with n-type redox-active carboxyl ( $\text{C}=\text{O}$ ) groups exchanging electrons at ideal potentials for an aqueous battery anode. Despite PTCDI's previous successful implementation in aqueous sodium-ion, potassium-ion, and magnesium-ion batteries (SIBs, PIBs, MIBs, respectively) [12–15], its use in ALIBs remains unexplored. A common theme of these aqueous PTCDI-based batteries has been to apply high C-rates and/or high salt concentrations. The former, however, could hide potential frailties of the material and pose a potential challenge for practical implementation when more realistic discharge times are relevant. Moreover, while the use of water-in-salt electrolytes

\* Corresponding author at: ALISTORE-ERI, CNRS FR 3104, Hub de l'Energie, 80039 Amiens Cedex, France.

\*\* Corresponding author at: Chimie du Solide et de l'Energie (CSE), Collège de France, UMR 8260, 75231 Paris Cedex 05, France.

E-mail addresses: [patrik.johansson@chalmers.se](mailto:patrik.johansson@chalmers.se) (P. Johansson), [grimauda@bc.edu](mailto:grimauda@bc.edu) (A. Grimaud).

<sup>1</sup> Shared first authorship.

(WISEs), where salt outweighs water in both volume and mass and typically harness large sulfonimide anions, can effectively suppress active material dissolution during cycling, high salt concentrations inherently introduce cost and sustainability concerns, contradicting the principles of aqueous batteries [16,17].

Herein, we first explore the electrochemical behavior of PTCDI with aqueous electrolytes of relatively moderate lithium salt concentrations (1.0–5.0 m) in half-cell configuration. The initial electrochemical response alludes to different redox processes with aqueous vs. organic electrolytes, unlike for SIBs and PIBs [12,18–20], and therefore we set out to investigate and provide insight into the charge storage mechanism using various *ex situ* and *in situ* analyses. Furthermore, in the context of ALIBs we, for the first time, demonstrate the electrochemical performance of PTCDI as an anode material in half-cell configuration using  $\text{LiFePO}_4$  as counter electrode, and its potential application in balanced full cells using spinel  $\text{LiMn}_2\text{O}_4$  as positive material.

## Materials and methods

### Electrolyte preparation

Electrolytes based on lithium bis(trifluoromethanesulfonyl)imide (LiTFSI) (99.9 %, Solvionic) and lithium sulfate ( $\text{Li}_2\text{SO}_4$ ) (anhydrous, 99.5 %, Sigma-Aldrich) were prepared with ultra-pure water (Millipore® Direct-Q® Purification,  $18.2 \text{ M}\Omega\cdot\text{cm}$  at  $25^\circ\text{C}$ ) in magnet stirred vials at *ca.*  $50^\circ\text{C}$ . The pH of the electrolytes was adjusted using bis(trifluoromethanesulfonyl)imide acid (HTFSI) (99.9 %, Solvionic) and sulfuric acid ( $\text{H}_2\text{SO}_4$ ) (99.999 %, Sigma-Aldrich), respectively.

### Active material synthesis

$\text{LiMn}_2\text{O}_4$  (LMO) active material (AM) powder was prepared according to [21] by heating at  $800^\circ\text{C}$  a stoichiometric mixture of  $\text{Li}_2\text{CO}_3$  (5 % excess) and  $\text{MnO}_2$  in air for 24 h, followed by two successive grinding and identical annealing sequences. The samples were cooled at a rate of  $2^\circ\text{C min}^{-1}$  until  $300^\circ\text{C}$  to ensure the proper oxygen stoichiometry.

### Electrode fabrication

The PTCDI AM ( $\geq 94\%$ , Thermo Fisher Scientific) based electrodes were made by first preparing a 3 wt% carboxymethyl cellulose (CMC) (Sigma-Aldrich) solution in ultra-pure water (Millipore® Direct-Q® Purification,  $18.2 \text{ M}\Omega\cdot\text{cm}$  at  $25^\circ\text{C}$ ) until complete dissolution in magnet stirred vials. PTCDI and carbon black (CB) (Super-P, Alfa Aesar) were thereafter manually mixed in a mortar and added to the CMC solution for 12 h. The slurry was casted on graphite foil (SGL Carbon) using a Doctor Blade followed by 12 h vacuum drying at  $80^\circ\text{C}$ . The electrode weight ratio PTCDI:CB:CMC was 75:15:10 with a final thickness of 30–50  $\mu\text{m}$  and an active material loading of 2–3  $\text{mg cm}^{-2}$ .

The freestanding PTCDI,  $\text{LiFePO}_4$  (LFP, Umicore) and LMO electrodes were prepared using the Bellcore method. AM, carbon super P (Csp, Timcal), and poly(vinylidene fluoride)-co-hexafluoropropylene (PVdF-HFP) (Solvay) in the ratio of 73:9:18 were hand ground and mixed in acetone to form a slurry. Dibutylphthalate (DBP, 99 % Sigma-Aldrich) was added as a plasticizer and the slurry was heated at  $50^\circ\text{C}$  under stirring. Then, the as-prepared slurry was poured into a petri dish (7 mm  $\varnothing$ ) and left to dry to form a film. The film was washed three times in diethyl ether (99% min, Alfa Aesar) and dried at  $60^\circ\text{C}$  under vacuum. Resulting loadings varied, much depending on the purpose of the electrodes, but generally PTCDI = 4–6  $\text{mg cm}^{-2}$ , LFP =  $\sim 20 \text{ mg cm}^{-2}$  and LMO = 4–6  $\text{mg cm}^{-2}$ .

### Physico-chemical characterization

The densities ( $\rho$ ) of the electrolytes were measured from  $20^\circ\text{C}$  to  $80^\circ\text{C}$

$^\circ\text{C}$  in steps of  $10 \pm 0.02^\circ\text{C}$  with an Anton Paar DMA 4500 M oscillation U-tube densitometer, where the U-tube resonates at different eigenfrequencies depending on the mass. A Lovis 2000 ME rolling ball viscometer module was used to measure the viscosities ( $\eta$ ) of the electrolytes at the same temperatures. The ion conductivities ( $\sigma$ ) were measured using a Mettler-Toledo SevenCompact S230 conductivity meter with a 12 mm InLab® 710 Cond probe with 4 Pt poles conductivity cell ( $\pm 0.5\%$ ), again at the same temperatures as controlled by a home-built thermoelectric set-up.

### Materials characterization

Free-standing PTCDI electrodes (5 mm  $\varnothing$ ) were pre-cycled to charged and discharged states by galvanostatic cycling (GC) in 2-electrode coin cells (CR2032) with freestanding oversized LFP counter electrodes (CE) (10 mm  $\varnothing$ ), and two Whatman cellulose filter separators (Grade 44, Sigma-Aldrich) (14 mm  $\varnothing$ ) using a Biologic VMP4 multichannel potentiostat/galvanostat or a Scribner Associates Incorporated 580 Battery Test System between 0.2 and 1.4 V at 1C. Post cycling, the electrodes were recovered, washed with 1 ml ultra-pure water and dried at  $60^\circ\text{C}$  for 12 h. *Ex situ* X-ray diffraction (XRD) was performed on electrodes put on top of Si single crystal low background sample holders and for the PTCDI powder in a standard sample holder levelled with the surface, using a Bruker D8 Discovery in the range  $5\text{--}35^\circ 2\theta$ .  $\text{Cu K}\alpha$  radiation was used with a Ni filter to cut  $\text{Cu K}\beta$  contributions, with two  $2.5^\circ$  sller slits to improve peak shapes. The incidence slit was set to Fixed Sample Illumination mode with 5 mm illumination, and an anti-scatter shield was placed 2.5 mm above the samples. The samples were measured with  $0.02^\circ$  increments and 2 s per step, summing up to 3150 s per scan, while rotated at 10 rpm.

Fourier-transform infrared (FTIR) vibrational spectra were obtained using a Bruker Alpha attenuated total reflection (ATR-FTIR) spectrometer and a Ge crystal, for the same electrodes as for the *ex situ* XRD. The spectra were recorded with  $2 \text{ cm}^{-1}$  resolution and 512 scans.

The scanning electron microscopy (SEM) images were taken with a JEOL 7800F Prime at an acceleration voltage of 6.0 kV and 10 mm working distance.

UV-Vis spectra were recorded on a Mettler Toledo UV5bio spectrometer using an absorption quartz cell across a wavelength range of 200–800 nm (Hellma analytics, Quartz Glass High Performance 200 – 2500 nm, 1 mm optical path length).

### Electrochemical and battery assessments

The GC and cyclic voltammetry (CV) studies were carried out on the same Biologic and Scribner instruments. The former was done in coin cells with carbon foil supported PTCDI working electrodes (WEs) (10 mm  $\varnothing$ ), freestanding oversized LFP CEs (10–14 mm  $\varnothing$ ), and two Whatman cellulose filter separators (16 mm  $\varnothing$ ) between 0.2 and 1.6 V at 0.25–10C. The latter was done with a 3-electrode Swagelok cell assembled with a PTCDI WE, a free-standing LFP CE, both 10 mm  $\varnothing$ , and an Ag/AgCl reference electrode (RE) (5 mm  $\varnothing$ , 0.127 mm silver foil, Alfa Aesar/AgCl ink, ALS Japan) together with the same separators between  $-1.0 \text{ V}$  and  $0.15 \text{ V}$  vs. Ag/AgCl at  $0.2 \text{ mV s}^{-1}$ . Balanced PTCDI|LMO full cells were assembled with 10 mm  $\varnothing$  and the PTCDI : LMO is balanced in a weight ratio of 1:1.1. 40  $\mu\text{l}$  of electrolyte was used for all cells, Swagelok and coin cells. A beaker cell utilising self-standing PTCDI, LFP and Ag/AgCl reference electrode was used for phenol red (Sigma Aldrich) measurements, one drop of phenol red was added to 10 mL of electrolyte, the cell was purged with Ar gas and a magnetic stirrer was added to ensure the electrolyte was mixed during the measurement.

The specific capacity  $Q$  ( $\text{mAh g}^{-1}$ ) of the cells was calculated as:

$$Q = \frac{It}{m}, \quad (1)$$

where  $I$  (mA) is the discharge current,  $t$  (h) the discharge time, and  $m$  (g) is the mass of AM in the electrode.

The AM level specific energy density  $E$  (Wh kg<sup>-1</sup>) was then calculated as:

$$E = \frac{\int IV(t)dt}{3.6m}, \quad (2)$$

where,  $I$  (A) is the applied current,  $V$  (V) is the voltage of the cell,  $t$  (s) is the corresponding discharge time, and  $m$  (g) is the sum of the weight of AM in both electrodes [22].

The logarithm of the peak current ( $i_p$ ) was plotted vs. the sweep rate ( $v$ ), and the  $b$  parameter from:

$$\log i = b \cdot \log v + \log a, \quad (3)$$

was taken as the slope of the linearization and used to determine if the current originates from Faradaic redox reactions or non-Faradaic capacitive behaviour as the former would give a value of  $b \approx 0.5$ , and the latter  $b \approx 1.0$  [23,24].

For the electrochemical quartz crystal microbalance (EQCM-R) measurements, a diluted slurry (73:18:9 PTCDI:Csp:PVDF wt%) using NMP as a solvent was prepared and sonicated to ensure homogenous particle dispersion. This solution was subsequently sprayed onto 9 MHz QCM resonators (Bio-Logic) made from gold that were heated to 150 °C during the spraying process to evaporate the solvent upon contact and then heated to 200 °C for 30 min to melt the binder to ensure good film cohesion. The resonators modified with the PTCDI thin films were mounted in an airtight EQCM cell developed previously [25]. For the aqueous electrolytes the PTCDI coated EQCM electrode acted as WE, a Pt-rod coated with self-standing Bellcore LFP as CE, and Ag/AgCl (saturated K<sub>2</sub>SO<sub>4</sub>) as RE. For the measurements using organic electrolytes, Li metal was used as CE and RE. Each measurement used 2 mL of electrolyte. The EQCM measurements were performed using a S2 Bio-logic SP200 workstation coupled with a commercial SEIKO QCM922A microbalance, which permitted the resonance frequency ( $f$ ) to be monitored during electrochemical cycling. The scan rates used for aqueous electrolytes was 5 mV s<sup>-1</sup> between -1.0 V and 0.15 V vs. Ag/AgCl. For the CV utilised to determine  $b$ -values, the scan rate was taken between 1 and 20 mV s<sup>-1</sup>. For the organic cell, the scan rate was 0.2 mV s<sup>-1</sup> between a voltage range of 1.5 to 3.5 V vs. Li. Where applicable, i.e. when the  $\Delta f/\Delta R_m > 25$  Hz/ $\Omega$  [25,26], the Sauerbrey equation is used:

$$\Delta m = -\frac{A\sqrt{\rho_q\mu_q}}{2f_0^2}\Delta f = -C_f\Delta f \quad (4)$$

where  $A$  is the piezoelectrically active area (0.196 cm<sup>2</sup>),  $\rho_q$  is the density of quartz (2.648 g cm<sup>-3</sup>), and  $\mu_q$  is the shear modulus of the quartz crystal ( $2.947 \times 10^{11}$  g cm<sup>-1</sup> s<sup>-2</sup>),  $C_f$  is the sensitivity coefficient/calibration constant, which is  $1.23 \pm 0.03$  ng Hz<sup>-1</sup> and determined by Ag electrodeposition detailed in a previous study [26]. The estimation of the mass per electron (M. P. E.) is done by using the slope of the  $\Delta m$  vs.  $\Delta Q$  plots (Fig. 3), where  $M. P. E. = \frac{nF\Delta m}{\Delta Q}$ , where  $F$  is Faraday's constant and  $n$  is the number of electrons.

## Results & discussion

To begin with, CV, *ex situ* XRD, and *ex situ* FTIR spectroscopy were all used to assess the PTCDI electrode's reversibility with our electrolytes, the structural changes (if any) and the mechanisms at hand. Thereafter, the active charge carrier(s) was investigated by *in situ* EQCM and by studying the effect of charge carrier concentration on the redox potential, using the Nernst equation. Furthermore, in 3-electrode and 2-electrode half-cells, the electrochemical performance of PTCDI as an ALIB anode was evaluated by applying CV and GC from low to high scan rates. Finally, proof-of-concept PTCDI||LMO ALIB full cells were assembled

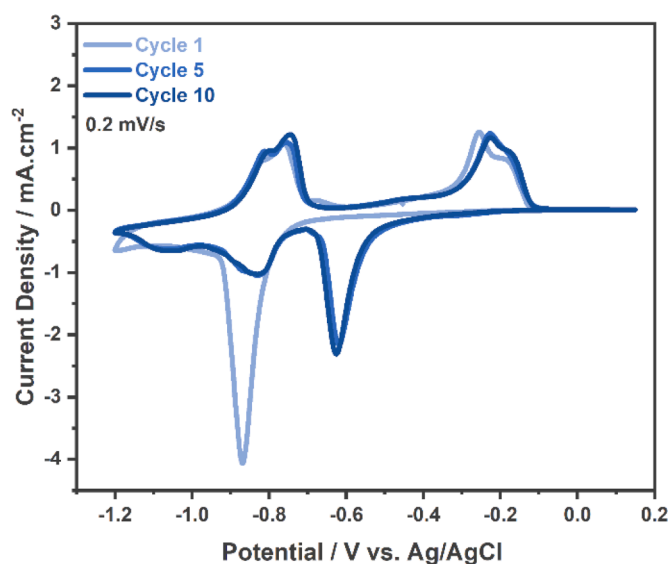


Fig. 1. Cyclic voltammogram of the PTCDI electrode using a 1.0 m LiTFSI(aq) electrolyte in a 3-electrode Swagelok cell.

and cycled long term to showcase the practical implementation of PTCDI.

### Reversibility with aqueous electrolytes

To probe the feasibility of using PTCDI under non-WISE conditions, 1.0 – 5.0 m LiTFSI(aq) and 1.0 – 3.0 m Li<sub>2</sub>SO<sub>4</sub>(aq) were targeted as potential electrolytes and characterised (Fig. S1). To probe PTCDI at the lowest concentration, 1.0 m LiTFSI(aq) electrolyte was chosen and the first cycle of the CV reveals a single reduction peak at -0.85 V (vs. Ag/AgCl) and two closely positioned oxidation peaks at -0.85 and -0.80 V, alongside another oxidation peak at -0.2 V (Fig. 1). In the subsequent cycles, two reduction peaks emerge at -0.63 V and -0.85 V, while the oxidation peaks remain the same, very similar to the behaviour of PTCDI with a saturated NaTFSI(aq) electrolyte [18]. This activation is also present for PTCDI with organic electrolytes (Fig. S2) and is yet to be fully understood. Moreover, since the redox behaviour differs when applying aqueous and organic electrolytes (Fig. S3), which is not the case for sodium and potassium based electrolytes [12,18–20], it raises the question of whether the redox mechanism for PTCDI also differs with different solvents, or if there could be structural changes and/or different pathways unique to aqueous electrolytes and/or alternative charge carriers present, such as H<sup>+</sup>.

By FTIR spectroscopy both pure PTCDI and pristine electrodes were shown to display characteristic absorption bands at 1277 cm<sup>-1</sup>, 1363 cm<sup>-1</sup>, 1685 cm<sup>-1</sup>, and 3154 cm<sup>-1</sup>, corresponding to the C–N, C=O, and N–H stretching vibrations of the imide groups, respectively (Fig. 2a). Additionally, they show stretching vibrations of the perylene ring and aromatic C–H at 1589 cm<sup>-1</sup>, 2857 cm<sup>-1</sup>, and 3041 cm<sup>-1</sup>, respectively (Fig. 2a) [27]. Upon the first charge, i.e., reduction of PTCDI, significant shifts and/or intensity changes are observed for all peaks, suggesting a significant transformation in the local environment. The significant reduction in the C=O and aromatic C–H bands accompanied by a downward shift of the perylene ring band indicate a decreased  $\pi$ -electron delocalization, which is consistent with enolization of the C=O group by cation coordination, following the reaction C=O  $\rightarrow$  C–O–Li via delocalisation of the conjugated ring, as previously demonstrated for both aqueous and organic electrolytes [27]. During the following discharge, i.e., oxidation of PTCDI, most bands recover their original intensities and positions, indicating de-enolization and thus a reversible redox mechanism. The merging of the 1685 cm<sup>-1</sup> C=O vibration from a double to a single peak is similar to with organic electrolytes [28], and



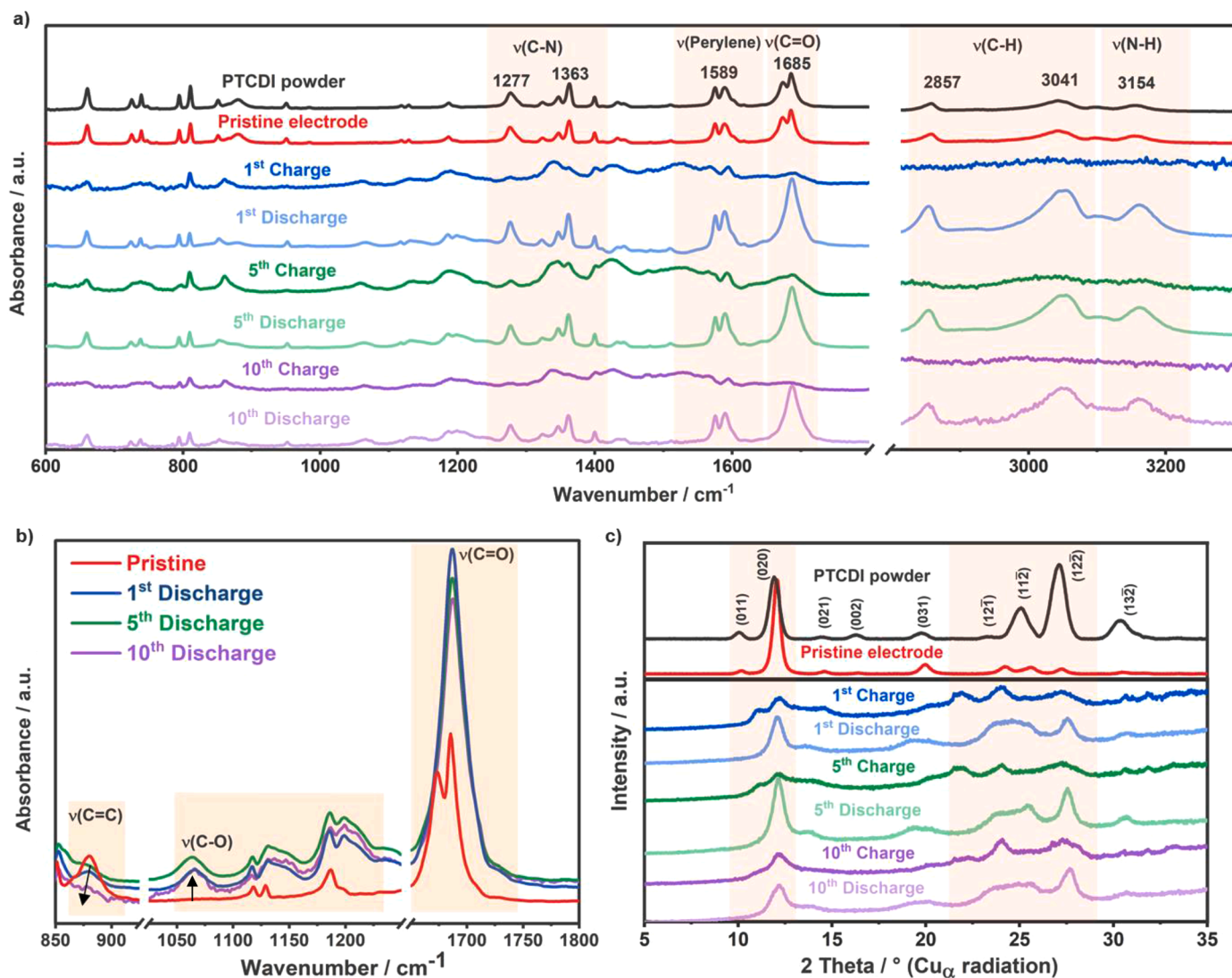


**Fig. 2.** Ex situ a) full FTIR spectra b) 600 – 1800  $\text{cm}^{-1}$  region of the FTIR spectra and c) X-ray diffractograms of free-standing PTCDI electrodes cycled with 1.0 m  $\text{LiTFSI}_{(\text{aq})}$ .

the new 1065  $\text{cm}^{-1}$  peak which remains during discharge has previously been associated with a C–O bond [29] (Fig. 2b). Meanwhile, the decrease in intensity of the 875  $\text{cm}^{-1}$  C=C vibration indicates a potential

change to the delocalisation of the structure (Fig. 2b). These IR changes between the pristine and the subsequent discharged states, also considering the irreversible capacity of the first cycle (Fig. S3), point to

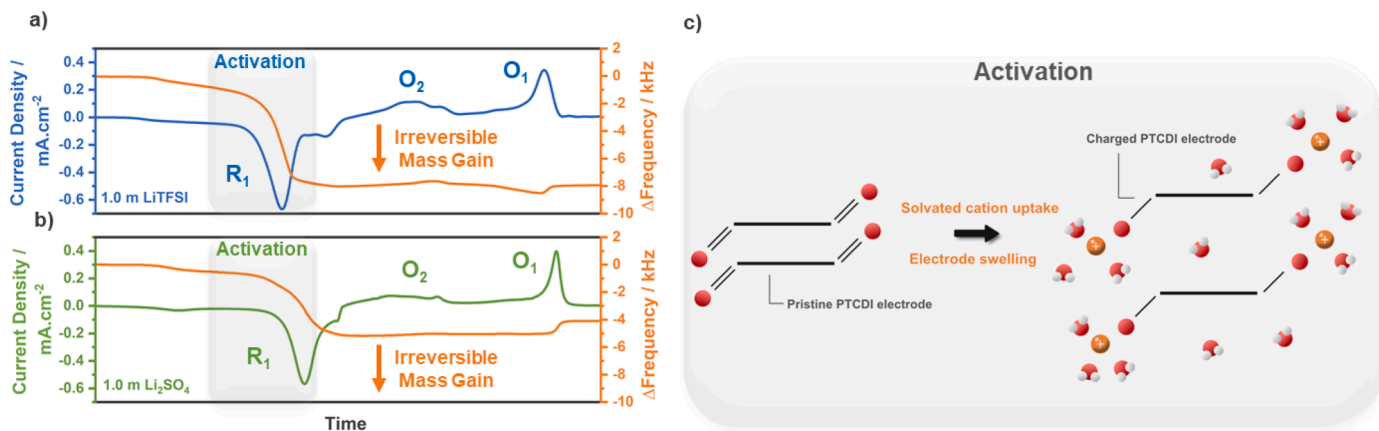


**Fig. 3.** Cycle 1 EQCM response of PTCDI using a) 1.0 m  $\text{LiTFSI}_{(\text{aq})}$  and b) 1.0 m  $\text{Li}_2\text{SO}_{4(\text{aq})}$  electrolytes, respectively, where  $R_1$  = first reduction peak and  $O_{1,2}$  = first and second oxidation peaks. c) Activation schematic of solvated  $\text{Li}^+$  uptake.

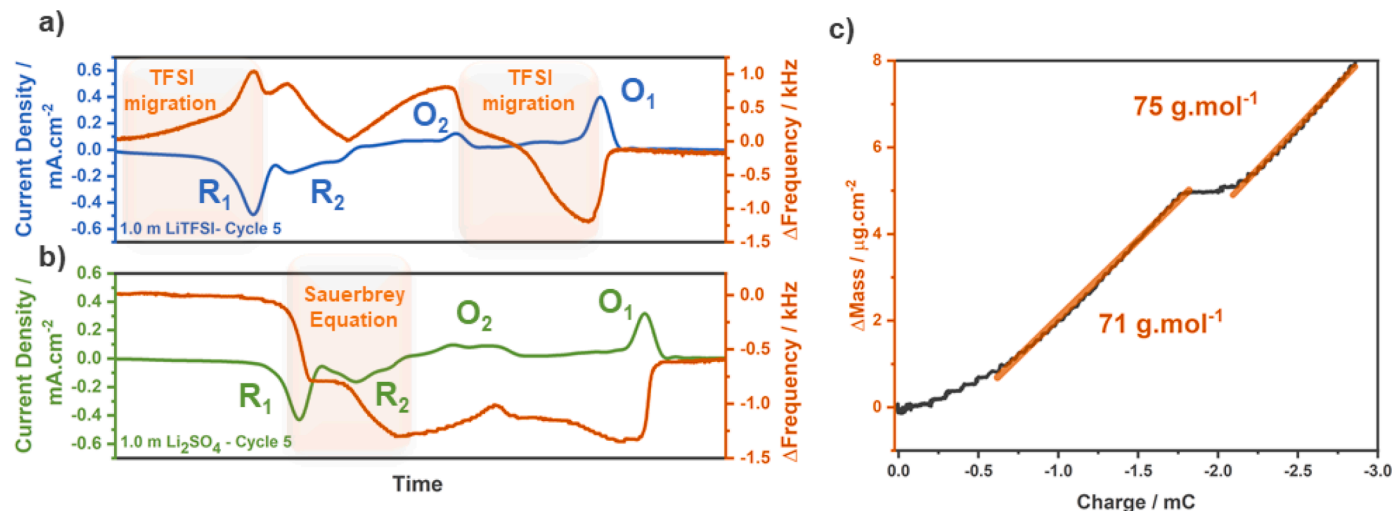


**Fig. 4.** a) EQCM response from the 5<sup>th</sup> cycle with 1.0 m LiTFSI(aq), b) 1.0 m Li<sub>2</sub>SO<sub>4</sub>(aq), and c)  $\Delta m$  vs.  $\Delta Q$  with linear fits to calculate the "molecular weights" for 1.0 m Li<sub>2</sub>SO<sub>4</sub>(aq).

some Li<sup>+</sup> remaining during discharge and is likely connected to the PTCDI electrode activation.

The X-ray diffractograms of the pure PTCDI, both in powder and electrode forms, match the expected crystal structure with the P12<sub>1</sub>/n1 space group in a monoclinic phase (Fig. 2c) [30]. Upon charging the (12 $\bar{1}$ ), (11 $\bar{2}$ ) and (12 $\bar{2}$ ) peaks undergo shifts to lower 2 $\theta$  angles, accompanied with an overall loss in crystallinity, but again this is reversible: upon discharge, the crystallinity returns and the aforementioned peaks shift back. The discharged pattern does, however, change slightly from the pristine state, with peak shifts and reduced crystallinity, indicating a potential alteration in the crystal structure; yet it remains uncertain whether this is due to structural activation or to the pre-measurement cleaning process. The loss and return of crystallinity upon charge/discharge occurs for cycles 5 and 10, indicating the very reversible process, in tandem with the *ex situ* FTIR spectroscopy. In addition, the SEM micrographs (Fig. S4) support the reversibility of the process. It is worth noting that an unexplained deposition or surface formation occurs on the PTCDI electrode in the early charged states that reversibly disappears during discharge. Moreover, a continuous merging of the elongated PTCDI crystals is observed upon cycling and this could very well be related to the structural activation and explain the

differences in the XRD patterns between the pristine and cycled electrodes.

#### Active charge carrier(s)

Although it has been established that the charge storage mechanism occurs via enolization of the C=O bond, further investigations are required to the identity of the charge carrier(s). Through *in situ* EQCM-R, which enables simultaneous measurement of motional resistance and frequency fluctuations, significant mass increases are observed during reduction for both electrolytes (Fig. 3a & 3b). This can be attributed to electrode swelling by the uptake of strongly solvated ions (Fig. 3c), such as Li<sup>+</sup> [31]. Upon oxidation the frequency does not fully recover, suggesting an irreversible process during the first cycle, which could explain the structural 'activation' of PTCDI. A comparable change occurs when using the non-aqueous 1.0 m LiTFSI(EC:PC) electrolyte, suggesting that this phenomenon is not exclusive to aqueous electrolytes (Fig. S5). The first cycle high motional resistance ( $R_m$ ),  $\Delta 200 \Omega$  for Li<sub>2</sub>SO<sub>4</sub>(aq) and  $\Delta 1000 \Omega$  for LiTFSI(aq) (Fig. S6), can depend on many factors such as: film roughness, electrolyte properties, mass changes, and electrode characteristics, and hence a high  $\Delta R_m$  could be an indicator of structural

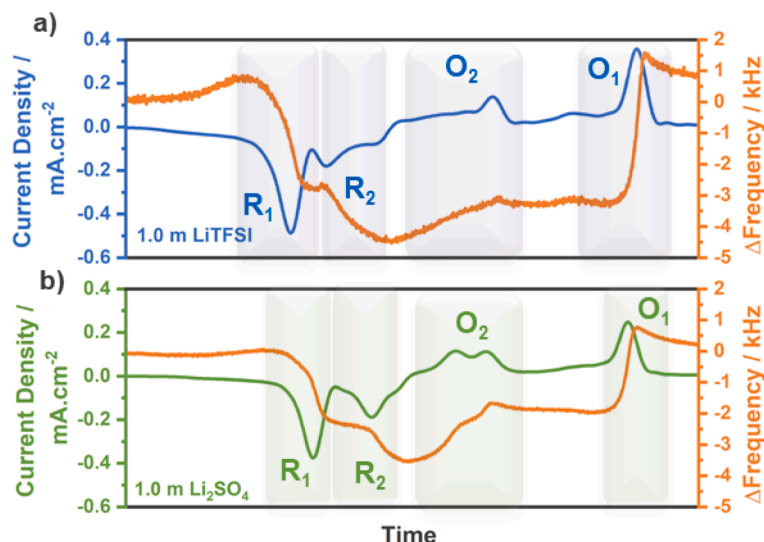


**Fig. 5.** EQCM responses from the 50<sup>th</sup> cycle using the a) 1.0 m LiTFSI(aq) and b) 1.0 m Li<sub>2</sub>SO<sub>4</sub>(aq) electrolytes.

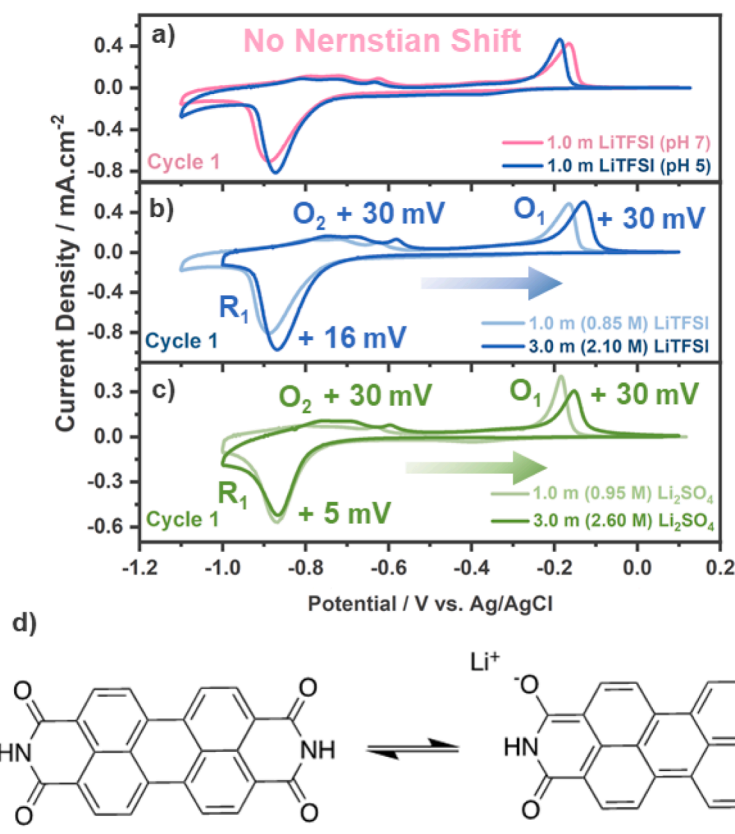


Fig. 6. 1<sup>st</sup> CV cycle of PTCDI with different a) pH, b) [LiTFSI<sub>(aq)</sub>], c) [Li<sub>2</sub>SO<sub>4(aq)</sub>], and d) the proposed charge storage mechanism.

changes. Unfortunately, a large  $\Delta R_m$  relative to  $\Delta f$  can disrupt the mass-frequency linearity, nullifying the use of the Sauerbrey equation (Eq. (4)) [25,26].

In the 5<sup>th</sup> cycle, the 1.0 m LiTFSI<sub>(aq)</sub> electrolyte data show an unusual response:  $f$  gain/mass loss before R<sub>1</sub>,  $f$  loss/mass gain before O<sub>1</sub>, indicating a redox process not involving typical cation de(intercalation)/coordination (Fig. 4a). The second redox feature (R<sub>2</sub>/O<sub>2</sub>) aligns more with cation (de)intercalation/coordination. The frequency fluctuations observed during R<sub>1</sub> and O<sub>1</sub> are limited to aqueous electrolytes as the response for the 1.0 m LiTFSI<sub>(EC:PC)</sub> electrolyte matches a typical one step cation (de)intercalation/coordination process (Fig. S7). Unfortunately, the low  $\Delta f/\Delta R_m$  ratio falls below the mass-frequency linearity threshold preventing mass quantification. Meanwhile, the 5<sup>th</sup> cycle for 1.0 m Li<sub>2</sub>SO<sub>4(aq)</sub> showcases the expected cation (de)intercalation/coordination response, with a  $\Delta f$  decrease for R<sub>1</sub> and R<sub>2</sub>, and a  $\Delta f$  increase for O<sub>1</sub> and O<sub>2</sub>, although there is an irreversible mass gain between O<sub>1</sub> and O<sub>2</sub> (Fig. 4b). During reduction for Li<sub>2</sub>SO<sub>4(aq)</sub>  $\Delta f/\Delta R_m$  is  $>25$  Hz/ $\Omega$  (Fig. S8), allowing the use of the Sauerbrey equation (Eq. 5). The calculated “molecular weights” were 71 g mol<sup>-1</sup> for R<sub>1</sub> and 75 g mol<sup>-1</sup> for R<sub>2</sub>, which points to solvated Li<sup>+</sup> with 3.6 and 3.8 water molecules on average, respectively (Fig. 4c). The different response between LiTFSI and Li<sub>2</sub>SO<sub>4</sub> could possibly be attributed to the hydrophobic/chaotropic character of [TFSI]<sup>-</sup> compared to the kosmotropic/hydrophilic SO<sub>4</sub><sup>2-</sup> anions. Indeed, a recent study of PTCDI in dilute aqueous Na-based electrolytes, observed that hydrophobic/chaotropic anions exhibited an enhanced presence near the electrode surface. In contrast, kosmotropic anions showed a diminished presence near the electrode surface [32]. Hence, TFSI anions could be accumulating near the surface, resulting in electrostatic interaction with PTCDI and consequently influencing the frequency responses observed in cycle 5. On the other hand, SO<sub>4</sub><sup>2-</sup> anions are not present near the surface, and as a result, such frequency responses are not observed. While this hypothesis is interesting, further studies are certainly required to understand the effects of

kosmo/chaotropic anions.

Interestingly, by the 50<sup>th</sup> cycle, the anomalous  $\Delta f$  fluctuations dissipate, revealing a more typical response for a two-step cation (de) intercalation/coordination process for both 1.0 m LiTFSI<sub>(aq)</sub> and Li<sub>2</sub>SO<sub>4(aq)</sub> (Fig. 5) indicating that the differences between electrolytes are limited to the early cycles, but the low  $\Delta f/\Delta R_m$  ratios persist, even for the Li<sub>2</sub>SO<sub>4</sub> based electrolyte (Fig. S9). While further studies using EQCM-D, which has the added function of measuring dissipation, rather than EQCM-R, may better catch the early cycle  $\Delta f$  fluctuations and explain the electrolyte differences and provide insights also into electrode viscoelastic properties, we do note that whenever there is a peculiar  $\Delta f$  response, this is usually accompanied by a large variation in  $\Delta R_m$ . Dissolution and/or precipitation seems not to be the cause, as no absorption bands are observed in the dissolution test with the 1.0 m LiTFSI<sub>(aq)</sub> electrolyte, quite unlike the situation when using DMSO (Fig. S10), in accordance with previous studies [33].

While solvated Li<sup>+</sup> appears to be the main charge carrier, the “co-insertion” of water could result in other charge carriers being active, such as H<sup>+</sup>. Indeed, a recent study on PTCDI in dilute neutral aqueous electrolytes attributes the EQCM response to water absorption, where H<sup>+</sup> is thought to intercalate via OH<sup>-</sup> dissociation, resulting in an overall mass loss during reduction [34]. To test for this here, the pH during cycling was probed using phenol red, but there was no visible colour change. UV-Vis spectroscopy was applied to reveal even more subtle colour changes, but no shifts were observed (Fig. S11), leading us to conclude that there was no release of OH<sup>-</sup>, casting doubt on the aforementioned mechanism to occur also for PTCDI. Moreover, if H<sup>+</sup> intercalation would occur via an alternative mechanism, a Nernstian shift (+59 mV/decade) in the redox potentials should occur, but a two-order magnitude [H<sup>+</sup>] change (from pH 7 to pH 5) does not affect the redox potential (Fig. 6a). Conversely, changing the [Li<sup>+</sup>] from 1.0 to 3.0 m LiTFSI<sub>(aq)</sub> electrolytes resulted in a redox shift of +16 mV on R<sub>1</sub> and +30 mV on O<sub>1</sub> and O<sub>2</sub> which is in line with the expected +12 mV and +23 mV

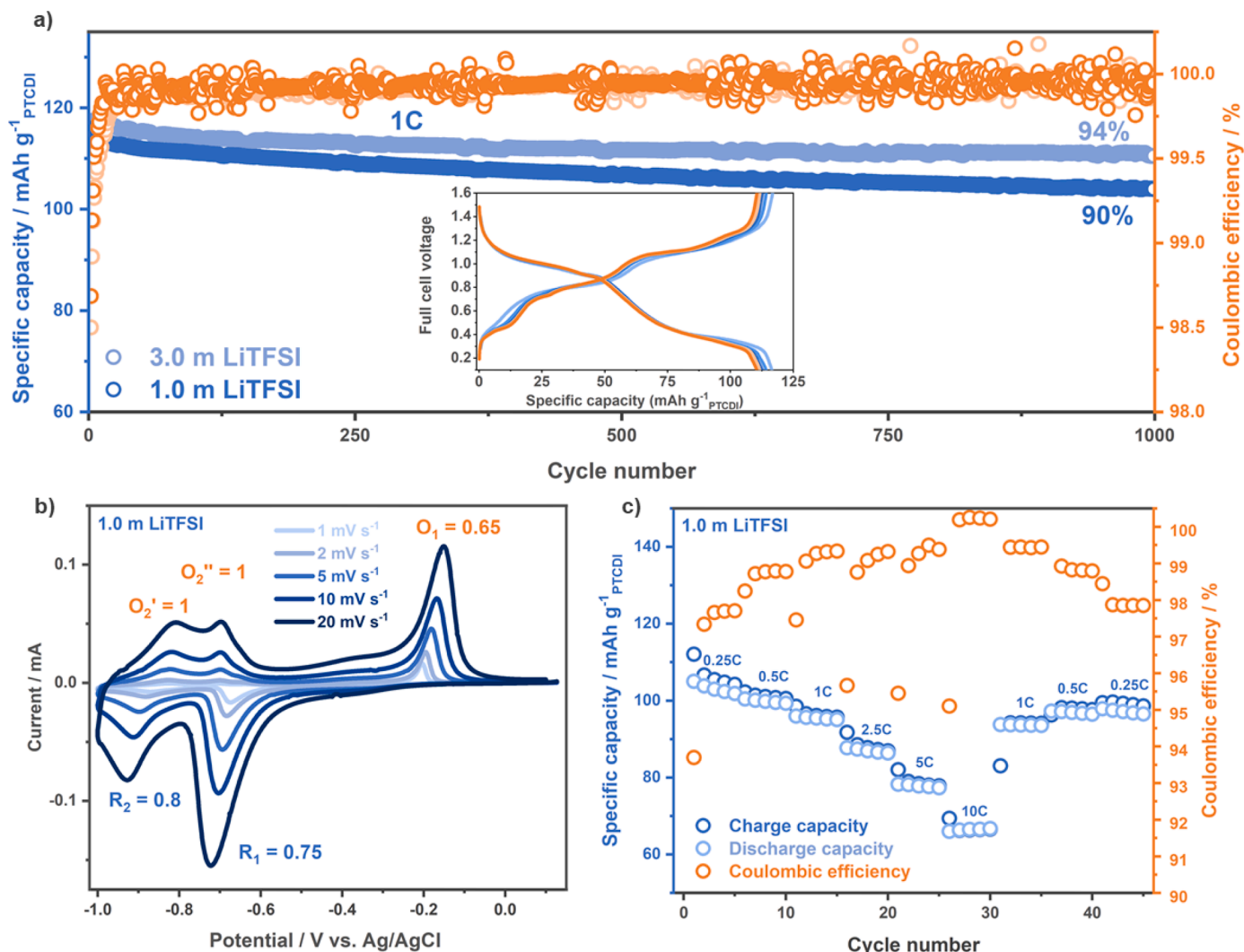


**Fig. 7.** PTCDI electrode a) long term cycling vs. LFP (coin cell, pseudo half-cell), b) CV and b-values from Eq. (3) cycled vs. LFP (EQCM cell, 3-electrode half-cell) and c) rate capability cycled vs. LFP (coin cell, pseudo half-cell).

**Table 1**

Comparison of aqueous PTCDI half-cells. C-rates are calculated relative to the theoretical capacity of PTCDI ( $137 \text{ mAh g}^{-1}$ ).

Electrolyte	C-rate	Capacity Retention	Ref.
1.0 M $\text{NaNO}_3(2:1 \text{ Glycerol:H}_2\text{O})$	0.1 $\text{A g}^{-1}$ ( $\sim 0.73\text{C}$ )	75 %@100	[35]
1.0 M $(\text{NH}_4)_2\text{SO}_4$	10C	90 %@400	[36]
22.0 m KOTf	20C	77 %@1000	[12]
22.0 m KOTf + 0.2 m FeOTf	1 $\text{A g}^{-1}$ ( $\sim 7.3\text{C}$ )	80 %@200	[13]
$\text{K(FSA)}_{0.6}(\text{OTf})_{0.4}1\cdot 0\text{H}_2\text{O}$	1 $\text{A g}^{-1}$ ( $\sim 7.3\text{C}$ )	100 %@200	[37]
5.0 m $\text{MgCl}_2$ + 2.0 m TBMACl	0.05 $\text{A g}^{-1}$ ( $\sim 0.365\text{C}$ )	64 %@100	[38]
0.5 M $\text{Mg}(\text{NO}_3)_2$	0.5 $\text{A g}^{-1}$ ( $\sim 3.65\text{C}$ )	87 %@10,000	[15]
1.0 m LiTFSI	0.137 $\text{A g}^{-1}$ (1C) 0.027 $\text{A g}^{-1}$ (0.2C)	90 %@1000 76 %@450	This work

Nernstian shifts (Fig. 6b, Supplementary Eq. 1 & 2). Shifts of +5 mV for  $R_1$  and +30 mV for  $O_1$  and  $O_2$  is observed for the 1.0 to 3.0 m  $\text{Li}_2\text{SO}_4(\text{aq})$  electrolytes and while  $R_1$  is slightly lower than the expected +13 mV,  $O_1$  and  $O_2$  is very close to the expected +26 mV shifts (Fig. 6c, Supplementary Eq. 3 & 4). Altogether, these findings strongly suggest solvated  $\text{Li}^+$  to be the primary charge carrier following the mechanism in Fig. 6b,

and as no alternative charge carriers to the best of our knowledge are present, we must conclude that the redox mechanism solely involves  $\text{Li}^+$ .

### Electrochemical performance

To study the electrochemistry of the PTCDI electrode, we first start by cycling *versus* an oversized LFP cathode with low-medium concentrated electrolytes. The PTCDI||LFP pseudo half-cell manages to deliver ca.  $117 \text{ mAh g}^{-1}$  in the 2<sup>nd</sup> cycle, close to the theoretical  $137 \text{ mAh g}^{-1}$  based on the uptake of 2  $\text{Li}^+$  (Fig. 7a). The cells exhibit excellent capacity retention with LiTFSI(aq) at relatively low cycling rates, exemplifying the cycling stability (Fig. 7a, Fig. S12, Fig. S15). In contrast, cells with  $\text{Li}_2\text{SO}_4(\text{aq})$  display severe capacity fading, highlighting the superior stability of the chaotropic  $[\text{TFSI}]^-$  compared to the kosmotropic nature of  $\text{SO}_4^{2-}$ , as observed for PTCDI (Fig. S13) [32]. Compared with previous aqueous PTCDI studies, applying PTCDI with LiTFSI(aq) offers one of the best capacity retentions reported so far (Table 1). This was achieved without resorting to the extreme WISE salt concentrations and at a comparably low rate. A self-discharge test reveals a  $2 \text{ mAh g}^{-1}$  discharge capacity loss after a 20 h OCV (Fig. S14), and while this represents a decreased Coulombic efficiency compared with continuous cycling, it is still low and emphasizes the material's stability.

To gain a deeper understanding of the charge storage mechanism — whether capacitive or diffusion-limited — a methodology previously



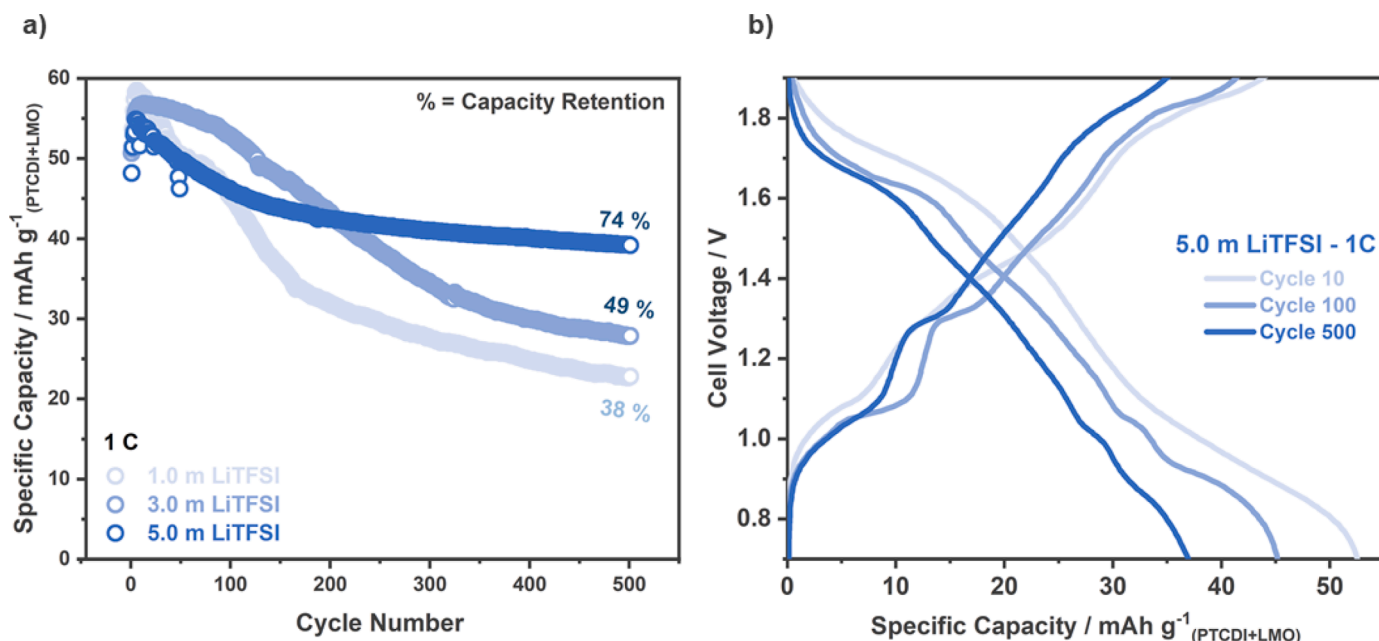


Fig. 8. a) Long-term cycling of balanced PTCDI||LMO full cells (coin cells) and b) the corresponding potential curves for 5.0 m LiTFSI<sub>(aq)</sub>.

developed by Dunn and coworkers [39] is employed (see Materials and Methods). The  $b$ -values extracted from this methodology demonstrate a mixture of faradaic ( $b = 0.5$ ) and non-faradaic ( $b = 1$ ) reaction mechanisms, with the first reduction peak ( $R_1$ ) and the first oxidation peak ( $O_1$ ) displaying a mixture of both mechanisms, while the second peaks ( $R_2$ ,  $O_2'$ , and  $O_2''$ ) are more non-faradaic, or pseudocapacitive (Fig. 7b) [40]. This is in line with previous studies of PTCDI using aqueous Na<sup>+</sup> and Zn<sup>2+</sup> conducting electrolytes [18,41], and the influence of a more capacitive controlled reaction mechanism should enable the PTCDI electrode to exhibit strong rate performance. This was evaluated and electrode does indeed retain a large amount of its initial capacity even up to 10C (Fig. 7c). The rate retention is comparable with previous studies using PTCDI with aqueous electrolytes, although we note few other studies apply rates <1C [12,15,36].

Finally, the PTCDI||LMO full cells with 1.0, 3.0, and 5.0 m LiTFSI<sub>(aq)</sub> electrolytes (Fig. 8a) show rather poor capacity retention for the 1.0 and 3.0 m electrolytes, which is attributed to the instability of LMO with aqueous electrolytes, while the 5.0 m electrolyte performs much better: a nominal voltage of 1.47 V, an energy density of 71 Wh kg<sup>-1</sup> (PTCDI+LMO, 10th cycle), and a capacity retention of 74 %@500 (Fig. 8b). While the salt concentration is rather high, diluents and additives can be employed to not only reduce the salt concentration, but also to mitigate the dissolution of LMO. We also acknowledge that Mn is a critical raw material (albeit in the lowest “very low” risk group) [4], but stress that these cells serve as a proof-of-concept to demonstrate a practical implementation of PTCDI for less expensive and more sustainable ALIBs as compared to WISE based batteries.

## Conclusions

The electrochemical behaviour and performance of PTCDI was herein studied and for the first time applied for ALIBs. Despite the different redox responses using organic and aqueous electrolytes, we can still conclude Li<sup>+</sup> to be the primary charge carrier, albeit with a slightly different mechanism. Furthermore, the electrochemical performance of PTCDI in half-cells and proof-of-concept full cells showcase the high stability with aqueous electrolytes and highlights its anode material capabilities for ALIBs. Altogether, this study aims to broaden the scope of ALIBs by implementing non-typical materials and electrolytes, leading to more sustainable and safe electrochemical energy storage.

## CRediT authorship contribution statement

**John Brown:** Conceptualization, Methodology, Investigation, Data curation, Formal analysis, Visualization, Writing – original draft. **Martin Karlsmo:** Conceptualization, Methodology, Investigation, Data curation, Formal analysis, Visualization, Writing – original draft. **Ezzoubair Bendadesse:** Investigation, Formal analysis. **Patrik Johansson:** Funding acquisition, Conceptualization, Project administration, Supervision, Resources, Writing – review & editing. **Alexis Grimaud:** Funding acquisition, Conceptualization, Project administration, Supervision, Resources, Writing – review & editing.

## Declaration of competing interest

The authors declare that they have no known competing financial interests or personal relationships that could have appeared to influence the work reported in this paper.

## Acknowledgements

J. B., P. J. and A. G. as a part of the DESTINY PhD programme acknowledges funding from the European Union’s Horizon 2020 research and innovation programme under the Marie Skłodowska-Curie grant agreement No: 945357. M. K. and P. J. would also like to express their appreciation to the Swedish Research Council for Sustainable Development (FORMAS), grant #2018-01450, and the Swedish Research Council (VR), grant #2021-00613, for supporting this work. We extend our gratitude to Dr. Sajid Alvi for carrying out the SEM measurements. Additionally, we express our appreciation to Prof. Jean-Marie Tarascon for synthesising the LMO particles and for fruitful discussions.

## Supplementary materials

Supplementary material associated with this article can be found, in the online version, at [doi:10.1016/j.ensm.2024.103218](https://doi.org/10.1016/j.ensm.2024.103218).

## References

- [1] W. Li, J.R. Dahn, D.S. Wainwright, Rechargeable lithium batteries with aqueous electrolytes, *Science* (80-) 264 (1994) 1115–1118, <https://doi.org/10.1126/SCIENCE.264.5162.1115>.

- [2] T.B. Schon, B.T. McAllister, P.-F. Li, D.S. Seferos, The rise of organic electrode materials for energy storage, *Chem. Soc. Rev.* 45 (2016) 6345, <https://doi.org/10.1039/c6cs00173d>.
- [3] Y. Lu, J. Chen, Prospects of organic electrode materials for practical lithium batteries, *Nat. Rev. Chem.* 43 (4) (2020) 127–142, <https://doi.org/10.1038/s41570-020-0160-9>, 2020.
- [4] E. Commission, I. Directorate-General for Internal Market Entrepreneurship and SMEs, M. Grohol, C. Veeh, Study on the critical raw materials for the EU 2023 – Final report, *Publicat. Office Europ. Union* (2023), <https://doi.org/10.2873/725585>.
- [5] Y. Liang, Y. Yao, Designing modern aqueous batteries, *Nat. Rev. Mater.* 82 (8) (2022) 109–122, <https://doi.org/10.1038/s41578-022-00511-3>, 2022.
- [6] G.J. Wang, L.C. Yang, Q.T. Qu, B. Wang, Y.P. Wu, R. Holze, An aqueous rechargeable lithium battery based on doping and intercalation mechanisms, *J. Solid State Electrochem.* 14 (2010) 865–869, <https://doi.org/10.1007/S10008-009-0869-3>.
- [7] H. Qin, Z.P. Song, H. Zhan, Y.H. Zhou, Aqueous rechargeable alkali-ion batteries with polyimide anode, *J. Power Sources.* 249 (2014) 367–372, <https://doi.org/10.1016/j.jpowsour.2013.10.091>.
- [8] L. Chen, W. Li, Z. Guo, Y. Wang, C. Wang, Y. Che, Y. Xia, Aqueous lithium-ion batteries using O 2 self-elimination polyimides electrodes, *J. Electrochem. Soc.* 162 (2015) A1972–A1977, <https://doi.org/10.1149/2.0101510jes>.
- [9] X. Han, C. Chang, L. Yuan, T. Sun, J. Sun, Aromatic carbonyl derivative polymers as high-performance Li-ion storage materials, *Adv. Mater.* 19 (2007) 1616–1621, <https://doi.org/10.1002/adma.200602584>.
- [10] W. Luo, M. Allen, V. Raju, X. Ji, An organic pigment as a high-performance cathode for sodium-ion batteries, *Adv. Energy Mater.* 4 (2014) 1400554, <https://doi.org/10.1002/aenm.201400554>.
- [11] M. Karlsmo, R. Bouchal, P. Johansson, High-performant all-organic aqueous sodium-ion batteries enabled by PTCDA electrodes and a hybrid Na/Mg electrolyte, *Angew. Chemie Int. Ed.* 60 (2021) 24709–24715, <https://doi.org/10.1002/anie.202111620>.
- [12] L. Jiang, Y. Lu, C. Zhao, L. Liu, J. Zhang, Q. Zhang, X. Shen, J. Zhao, X. Yu, H. Li, X. Huang, L. Chen, Y.S. Hu, Building aqueous K-ion batteries for energy storage, *Nat. Energy.* 4 (2019) 495–503, <https://doi.org/10.1038/s41560-019-0388-0>.
- [13] J. Ge, L. Fan, A.M. Rao, J. Zhou, B. Lu, Surface-substituted Prussian blue analogue cathode for sustainable potassium-ion batteries, *Nat. Sustain.* 53 (5) (2021) 225–234, <https://doi.org/10.1038/s41893-021-00810-7>, 2021.
- [14] Z. Huang, T. Wang, X. Li, H. Cui, G. Liang, Q. Yang, Z. Chen, A. Chen, Y. Guo, J. Fan, C. Zhi, Z. Huang, T. Wang, X. Li, H. Cui, G. Liang, Q. Yang, Z. Chen, A. Chen, Y. Guo, J. Fan, C. Zhi, Small-dipole-molecule-containing electrolytes for high-voltage aqueous rechargeable batteries, *Adv. Mater.* 34 (2022) 2106180, <https://doi.org/10.1002/ADMA.202106180>.
- [15] B. Wen, C. Yang, J. Wu, J. Liu, W. Wang, J. Yang, X. Chi, Y. Liu, Water-induced 3D MgMn<sub>2</sub>O<sub>4</sub> assisted by unique nanofluidic effect for energy-dense and durable aqueous magnesium-ion batteries, *Chem. Eng. J.* 435 (2022) 134997, <https://doi.org/10.1016/J.CEJ.2022.134997>.
- [16] L. Drognet, A. Grimaud, O. Fontaine, J.M. Tarascon, Water-in-salt electrolyte (WiSE) for aqueous batteries: a long way to practicality, *Adv. Energy Mater.* 10 (2020) 2002440, <https://doi.org/10.1002/AENM.202002440>.
- [17] T.F. Burton, R. Jommongkol, Y. Zhu, S. Deebansok, K. Chitbankluai, J. Deng, O. Fontaine, Water-in-salt electrolytes towards sustainable and cost-effective alternatives: example for zinc-ion batteries, *Curr. Opin. Electrochem.* 35 (2022) 101070, <https://doi.org/10.1016/J.COELEC.2022.101070>.
- [18] Z. Huang, Y. Hou, T. Wang, Y. Zhao, G. Liang, X. Li, Y. Guo, Q. Yang, Z. Chen, Q. Li, L. Ma, J. Fan, C. Zhi, Manipulating anion intercalation enables a high-voltage aqueous dual ion battery, *Nat. Commun.* 121 (12) (2021) 1–11, <https://doi.org/10.1038/s41467-021-23369-5>, 2021.
- [19] W. Deng, Y. Shen, J. Qian, Y. Cao, H. Yang, A perylene diimide crystal with high capacity and stable cyclability for Na-ion batteries, *ACS Appl. Mater. Interfaces.* 7 (2015) 21095–21099, <https://doi.org/10.1021/acsami.5b04325>.
- [20] M. Xiong, W. Tang, B. Cao, C. Yang, C. Fan, A small-molecule organic cathode with fast charge-discharge capability for K-ion batteries, *J. Mater. Chem. A.* 7 (2019) 20127–20131, <https://doi.org/10.1039/C9TA06376E>.
- [21] J.M. Tarascon, W.R. McKinnon, F. Coowar, T.N. Bowmer, G. Amatucci, D. Guyomard, Synthesis conditions and Oxygen stoichiometry effects on Li insertion into the spinel LiMn<sub>2</sub>O<sub>4</sub>, *J. Electrochem. Soc.* 141 (1994) 1421–1431, <https://doi.org/10.1149/1.2054941>.
- [22] Z. Zhang, Y. Zhu, M. Yu, Y. Jiao, Y. Huang, Development of long lifespan high-energy aqueous organic||iodine rechargeable batteries, *Nat. Commun.* 131 (13) (2022) 1–11, <https://doi.org/10.1038/s41467-022-34303-8>, 2022.
- [23] H. Zhang, M. Hu, Q. Lv, Z.H. Huang, F. Kang, R. Lv, Advanced materials for sodium-ion capacitors with superior energy–power properties: progress and perspectives, *Small* 16 (2020) 1902843, <https://doi.org/10.1002/sml.201902843>.
- [24] H. Lindström, S. Södergren, A. Solbrand, H. Rensmo, J. Hjelm, A. Hagfeldt, S. E. Lindquist, Li<sup>+</sup> ion insertion in TiO<sub>2</sub> (anatase). 2. Voltammetry on nanoporous films, *J. Phys. Chem. B.* 101 (1997) 7717–7722, <https://doi.org/10.1021/JP970490Q>.
- [25] P. Lemaire, T. Dargon, D. Alves Dalla Corte, O. Sel, H. Perrot, J.M. Tarascon, Making advanced electrogravimetry as an affordable analytical tool for battery interface characterization, *Anal. Chem.* 92 (2020) 13803–13812, <https://doi.org/10.1021/acs.analchem.0c02233>.
- [26] E. Bendadesse, A.V. Morozov, A.M. Abakumov, H. Perrot, J.M. Tarascon, O. Sel, Deciphering the double-layer structure and dynamics on a model Li<sub>x</sub>MoO<sub>3</sub> interface by advanced electrogravimetric analysis, *ACS Nano* 16 (2022) 14907–14917, <https://doi.org/10.1021/acsnano.2c05784>.
- [27] X. Lei, Y. Zheng, F. Zhang, Y. Wang, Y. Tang, Highly stable magnesium-ion-based dual-ion batteries based on insoluble small-molecule organic anode material, *Energy Storage Mater* 30 (2020) 34–41, <https://doi.org/10.1016/J.ENSMS.2020.04.025>.
- [28] J. Chen, S. Gu, R. Hao, K. Liu, Z. Wang, Z. Li, H. Yuan, H. Guo, K. Zhang, Z. Lu, Unraveling the role of aromatic ring size in tuning the electrochemical performance of small-molecule imide cathodes for lithium-ion batteries, *ACS Appl. Mater. Interfaces.* 14 (2022) 44330–44337, <https://doi.org/10.1021/acsami.2c11138>.
- [29] P. Zhao, Y. Feng, T. Li, B. Li, L. Hu, K. Sun, C. Bao, S. Xiong, A. Matic, J. Song, Stable lithium metal anode enabled by high-dimensional lithium deposition through a functional organic substrate, *Energy Storage Mater* 33 (2020) 158–163, <https://doi.org/10.1016/J.ENSMS.2020.08.025>.
- [30] K. Tojo, J. Mizuguchi, Refinement of the crystal structure of 3, 4:9, 10-perylene-bis (dicarboximide), C<sub>24</sub>H<sub>10</sub>N<sub>2</sub>O<sub>4</sub>, at 263K, *Zeitschrift Fur Krist. - New Cryst. Struct* 217 (2002) 45–46, <https://doi.org/10.1524/ncrs.2002.217.1.45>.
- [31] S. Wang, F. Li, A.D. Easley, J.L. Lutkenhaus, Real-time insight into the doping mechanism of redox-active organic radical polymers, *Nat. Mater.* 181 (18) (2018) 69–75, <https://doi.org/10.1038/s41563-018-0215-1>, 2018.
- [32] A. Nimkar, K. Alam, G. Bergman, M.D. Levi, D.T. Major, N. Shpigel, D. Aurbach, Is ‘water in salt’ electrolytes the ultimate solution? achieving high stability of organic anodes in diluted electrolyte solutions via a wise anions selection, *Angew. Chemie.* (2023), <https://doi.org/10.1002/ANGE.202311373>.
- [33] M. Esmailpourfarkhani, K. Abnous, S.M. Taghdisi, M. Chamsaz, A novel turn-off fluorescent aptasensor for ampicillin detection based on perylenetetracarboxylic acid diimide and gold nanoparticles, *Biosens. Bioelect.* 164 (2020) 112329, <https://doi.org/10.1016/J.BIOS.2020.112329>.
- [34] S. Zhang, X. Zhao, Y. Zhang, Y. Zhao, T. Li, J. Liu, F. Huang, T. Lin, Insights on the proton mechanism in carbonyl-based organic electrode of neutral aqueous battery, *J. Power Sources.* 550 (2022) 232110, <https://doi.org/10.1016/J.JPOWSOUR.2022.232110>.
- [35] Y. Sun, Y. Zhang, Z. Xu, W. Gou, X. Han, M. Liu, C.M. Li, Dilute hybrid electrolyte for low-temperature aqueous sodium-ion batteries, *ChemSusChem* 15 (2022) e202201362, <https://doi.org/10.1002/CSSC.202201362>.
- [36] X. Wu, Y. Qi, J.J. Hong, Z. Li, A.S. Hernandez, X. Ji, Rocking-chair ammonium-ion battery: a highly reversible aqueous energy storage system, *Angew. Chemie. Int. Ed.* 56 (2017) 13026–13030, <https://doi.org/10.1002/ANGE.201707473>.
- [37] T. Hosaka, R. Takahashi, K. Kubota, R. Tatara, Y. Matsuda, K. Ida, K. Kuba, S. Komaba, Origin of enhanced capacity retention of aqueous potassium-ion batteries using monohydrate-melt electrolyte, *J. Power Sources.* 548 (2022) 232096, <https://doi.org/10.1016/J.JPOWSOUR.2022.232096>.
- [38] K. Il Kim, L. Tang, J.M. Muratli, C. Fang, X. Ji, A graphite PTCDI aqueous dual-ion battery, *ChemSusChem* 15 (2022) e202102394, <https://doi.org/10.1002/CSSC.202102394>.
- [39] J. Wang, J. Polleux, J. Lim, B. Dunn, Pseudocapacitive contributions to electrochemical energy storage in TiO<sub>2</sub> (anatase) nanoparticles, *J. Phys. Chem. C.* 111 (2007) 14925–14931, <https://doi.org/10.1021/jp074464w>.
- [40] A. González, E. Goikolea, J.A. Barrena, R. Mysyk, Review on supercapacitors: technologies and materials, *Renew. Sustain. Energy Rev* 58 (2016) 1189–1206, <https://doi.org/10.1016/J.RSER.2015.12.249>.
- [41] N. Liu, X. Wu, Y. Zhang, Y. Yin, C. Sun, Y. Mao, L. Fan, N. Zhang, N. Liu, X. Wu, Y. Zhang, Y. Yin, C. Sun, Y. Mao, L. Fan, N. Zhang, Building high rate capability and ultrastable dendrite-free organic anode for rechargeable aqueous zinc batteries, *Adv. Sci.* 7 (2020) 2000146, <https://doi.org/10.1002/ADVS.202000146>.